crystals

MDPI

Article

Effect of Zr, Zn, and Cu on Corrosion Resistance of As-Extruded Mg-3Sn-1Ca Alloy

Zheng Jia [1,2,*], Sichao Du [1] and Xiaowei Niu [2]

[1] College of Mechanical Engineering, Shenyang University, Shenyang 110044, China; sichao0125@163.com
[2] College of Environment, Liaoning Province Pollution Environmental Remediation Professional Technology Innovation Center & Shenyang Key Laboratory of Collaborative Technology Innovation for Industrial Pollution Reduction and Carbon Reduction, Shenyang University, Shenyang 110044, China; niuxiaowei@syu.edu.cn
* Correspondence: jz140@163.com

Abstract: TX31 (Mg-3Sn-1Ca) is an alloy with promising future applications. This study enhances the corrosion resistance of the TX31 alloy through the addition of Zr and Zn and compares the effects of individual Cu addition and Zn/Cu composite addition on the corrosion resistance of the TX31 alloy. This study investigates the corrosion properties of TX31 alloys, focusing on the effects of the grain size, second phase, corrosion product film, and texture intensity. The addition of Zr and Zn changed the second-phase area fraction, while Cu introduced a new Mg_2Cu phase. The TXZ311 alloy (Mg-3Sn-1Ca-1Zn) exhibited the best corrosion resistance, with a corrosion rate as low as 1.68 mm·year^{-1}, a significant reduction compared to other alloys. This improvement is attributed to its higher fraction of high-angle grain boundaries (HAGBs) and the enhanced stability of the corrosion product film. The TXK311 alloy (Mg-3Sn-1Ca-1Zr) showed superior corrosion resistance, with a rate of 2.97 mm·year^{-1}, due to its uniform and fine grain structure. In contrast, the TX31 alloy had the poorest corrosion resistance, with a corrosion rate of 3.66 mm·year^{-1}, due to its bimodal microstructure. The addition of Cu in the TXC311 (Mg-3Sn-1Ca-1Cu) and TXCZ3111 (Mg-3Sn-1Ca-1Cu-1Zn) alloys resulted in micro-galvanic corrosion between α-Mg and Mg_2Cu, which decreased the corrosion resistance.

Keywords: TX31 alloy; microstructure; corrosion properties; corrosion product film

check for updates

Citation: Jia, Z.; Du, S.; Niu, X. Effect of Zr, Zn, and Cu on Corrosion Resistance of As-Extruded Mg-3Sn-1Ca Alloy. *Crystals* **2024**, *14*, 1098. https://doi.org/10.3390/cryst14121098

Academic Editors: Jijo Christudasjustus, Rajeev Gupta, Mohammad Umar Farooq Khan and Ulises Martin Diaz

Received: 28 November 2024
Revised: 16 December 2024
Accepted: 18 December 2024
Published: 20 December 2024

Copyright: © 2024 by the authors. Licensee MDPI, Basel, Switzerland. This article is an open access article distributed under the terms and conditions of the Creative Commons Attribution (CC BY) license (https://creativecommons.org/licenses/by/4.0/).

1. Introduction

Due to their unique properties, Mg alloys are widely utilized in the aerospace and transportation sectors. However, their application is limited by poor corrosion resistance [1,2]. Improving the corrosion resistance of Mg alloys is an urgent task. The surfaces of Mg alloys can be covered with coatings, such as plasma electrolytic oxidation [3] and chemical conversion coatings [4], to reduce or eliminate their exposure to the external environment and improve corrosion resistance [5]. However, the preparation of these coatings is complex and requires significant processing time and cost. Consequently, microalloying emerges as a preferable alternative [6].

Research has shown that Mg-Sn-Ca alloys exhibit favorable corrosion resistance and excellent creep resistance, largely due to the presence of intermetallic phases such as $Ca_{2-x}Mg_xSn$. To enhance microstructural homogeneity, alloys containing 3% Sn and 1–2% Ca were subjected to extrusion processing. Analysis using optical microscopy (OM) and X-ray diffraction (XRD) revealed the consistent presence of phases like Mg_2Sn, $Ca_{2-x}Mg_xSn$, and $Ca_{2-x}Mg_xSn/Mg_2Ca$ in both the as-cast and extruded conditions. Notably, the extrusion process promoted significant recrystallization, leading to grain refinement. This microstructural improvement contributed to enhanced corrosion resistance in the extruded alloys, making their performance comparable to the widely used AZ91D alloy [7]. At

the same time, Mg-Sn-Ca alloys have attracted significant attention due to their excellent thermal characteristics. This is attributed to the formation of CaMgSn and Mg_2Sn heat-resistant phases, while calcium (Ca) refines the grains, thereby enhancing the alloy's performance at elevated temperatures [8]. The results of this study demonstrate that the corrosion resistance of the TX31 alloy is lower than that of the T3 (Mg-3Sn) alloy. Therefore, it is crucial to add alloying elements to reduce the corrosion rate of the TX31 alloy. Zirconium (Zr), zinc (Zn), and copper (Cu) are commonly used alloying elements in Mg. An appropriate amount of Zr and Zn can enhance the corrosion resistance of alloys by refining the grain size. For example, Wan et al. [9] demonstrated that $Mg_{97}Zn_1Y_{2-x}$ wt.% Zr (x = 0, 0.1, 0.3, 0.6) alloys containing Zr exhibited reduced corrosion rates compared to those without Zr. Wang [10] and Yin [11] demonstrated that the corrosion resistance of Mg alloys improves with the addition of Zr, which refines the grains. Ha et al. [12] reported that adding 1 wt.% Zn to Mg-Zn binary alloys provided optimal corrosion protection. Additionally, Lotfpour [13] found that adding 0.5 wt.% Cu decreased the corrosion rate of the Mg-Zn alloy.

To reduce the corrosion rate of the TX31 (Mg-3Sn-1Ca) alloy, the TXK311 (Mg-3Sn-1Ca-1Zr), TXZ311 (Mg-3Sn-1Ca-1Zn), TXC311 (Mg-3Sn-1Ca-1Cu), and TXCZ3111 (Mg-3Sn-1Ca-1Cu-1Zn) as-extruded alloys were developed in this study. This study focuses on the systematic enhancement of the corrosion resistance of the TX31 alloy by adding Zr, Zn, and Cu and compares the effects of individual Cu addition and Zn/Cu composite addition. While previous studies have primarily concentrated on the impact of single alloying elements, this research explores the synergistic effects of these elements, offering a comprehensive understanding of their influence on the microstructure, second-phase distribution, and texture intensity. Moreover, the relationship between these microstructural features and the corrosion behavior is thoroughly examined. The findings aim to provide a theoretical foundation for reducing the corrosion rate of the TX31 alloy.

2. Experimental Section

2.1. Material Preparation

The T3, TX31, TXK311, TXZ311, TXC311, and TXCZ3111 alloys were prepared using pure Mg (99.9 wt.%), pure Sn (99.9 wt.%), pure Zn (99.9 wt.%), pure Cu (99.9 wt.%), and intermediate alloys Mg-25% Ca and Mg-30% Zr. The Mg ingot was placed in a superheated crucible and heated to 750 °C. After the pure Mg in the melting furnace had completely melted, pure Cu was added following the removal of slag. The temperature was then lowered to 740 °C, and the intermediate alloy Mg-30% Zr was added after slag removal. The temperature was further lowered to 710 °C, followed by drossing and the addition of pure Sn, pure Zn, and the intermediate alloy Mg-25% Ca. After maintaining a temperature of 710 °C for 25 min, the Mg alloy was cast into molds of Ø 65 × 240 mm under a protective gas mixture of CO_2 and SF_6 (100:1). The naturally cooled Mg alloy ingots were homogenized at 400 °C for 24 h, and the ingots were subjected to water quenching for cooling. After the as-cast alloys underwent uniform heat treatment, the surface of the homogenized alloy was polished using a lathe to ensure a smooth, defect-free surface, thereby preventing defects after extrusion. The extrusion speed was set to 60 mm/min, with an extrusion ratio of 15:1 and a temperature of 300 °C. Prior to extrusion, both the homogenized alloy and the extrusion die were preheated to the corresponding temperature. Finally, the cast ingot was subjected to backward extrusion using a 600-ton four-column hydraulic press, resulting in Ø 12 mm bars. The chemical composition of the as-cast alloys was analyzed using an Inductively Coupled Plasma Atomic Emission Spectrometer (ICP-AES). Table 1 presents the chemical compositions of the six alloys.

Table 1. Chemical composition.

Alloy	Measured Composition (wt.%)					
	Mg	**Sn**	**Ca**	**Zr**	**Zn**	**Cu**
T3	Bal.	2.97	0	0	0	0
TX31	Bal.	3.14	1.02	0	0	0
TXK311	Bal.	3.08	1.03	0.6	0	0
TXZ311	Bal.	3.14	1.02	0	1.09	0
TXC311	Bal.	3.22	1.04	0	0	1.07
TXCZ3111	Bal.	3.18	1.04	0	1.07	1.04

2.2. Microstructure and Composition Characterization

Samples (10 mm × 10 mm × 6 mm) were cut from the as-extruded bars, as shown in Figure 1. The surface of the specimens was sequentially polished using SiC abrasive papers ranging from 400# to 5000# and subsequently subjected to mechanical polishing, achieving a smooth and uniform finish to ensure reliable testing conditions. The microstructure and phases were observed using optical microscopy (OM) and scanning electron microscopy with energy dispersive spectroscopy (SEM/EDS) at an accelerating voltage of 10 kV. Phase identification was conducted using X-ray diffraction (XRD). The crystal orientation and grain size of the microzone were analyzed using electron backscatter diffraction (EBSD) with a step size of 0.5 μm, and Channel 5 v5.12 software was utilized for data interpretation.

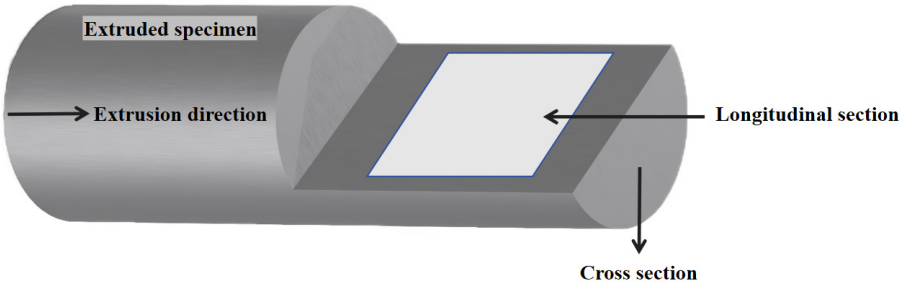


Figure 1. Metallographic sampling location.

2.3. Immersion Tests

The samples were immersed in a 3.5 wt.% NaCl solution (pH = 7) and corroded at 25 °C for 24 h. The volume of hydrogen evolved was measured every 2 h. To eliminate the influence of solution concentration changes on the experimental results, the 3.5 wt.% NaCl solution was replaced every 12 h. The corroded samples were subjected to ultrasonic cleaning in a chromate solution for 10 min. Each experiment was conducted five times to ensure reproducibility. The corrosion rate P_H (mm·year^{-1}) was calculated using Equation (1).

$$P_H = \frac{8.76 \times 10^4 \times \Delta V \times M}{A \times t \times \rho} \quad (1)$$

where P_H represents the corrosion rate, mm·year^{-1}; A denotes the exposed surface area of the alloy, cm^2; t indicates the immersion time, h; ρ represents the density of the alloy, g·cm^{-3}; ΔV denotes the H_2 volume, mL; and M represents the correlation between the hydrogen release rate and the mass loss rate of the alloy, 0.001083 g·mL^{-1}.

The electrochemical workstation model CHI660E was used to evaluate the corrosion performance of Mg alloys; the Mg alloy sample served as the working electrode (WE), the saturated calomel electrode was used as the reference electrode (RE), and the platinum electrode functioned as the counter electrode (CE). The back surface of the exposed area (10 mm × 10 mm) was connected via a wire, and all other surfaces, except the working surface, were sealed with epoxy resin. The prepared working electrode was immersed in a 3.5 wt.% NaCl solution for 3600 s to obtain a stable open circuit potential (OCP). Polarization

tests were then conducted within the potential range of −500 to 500 mV (relative to OCP) at a scan rate of 1 mV/s. In addition, electrochemical impedance spectroscopy (EIS) was performed within the frequency range of 1000 kHz to 0.01 Hz, with a disturbance voltage of 10 mV. The data fitting analysis was performed using ZView v3.1 software. The corrosion current density (i_{corr}) and the self-corrosion potential (E_{corr}) were obtained by extrapolating the Tafel plot from the polarization curves. Equation (2) describes the effect of i_{corr} (mA·cm^{-2}) on P_i (mm·year^{-1}) [14].

$$P_i = 22.85 i_{corr} \quad (2)$$

3. Results

3.1. Materials and Microstructure Characterization

Figures 2 and 3 depict the XRD patterns and SEM images of the alloys, respectively. According to the XRD analysis, only the Mg_2Sn phase was detected in the T3 alloy, while only the CaMgSn phase was identified in the TX31, TXK311, and TXZ311 alloys. In contrast, both the CaMgSn and Mg_2Cu phases were observed in the TXC311 and TXCZ3111 alloys. As observed in Figure 3, the white particles were aligned along the extrusion direction (ED). This is attributed to the fragmentation of the second phase during the extrusion process, resulting in fine, micron-sized second-phase particles, which were aligned into linear second-phase bands due to the plastic flow of the Mg matrix. The second-phase particles were quantified as shown in Table 2, and the EDS data from the SEM images are presented in Table 3. The area fraction of white particles in the TX31 alloy was 7.5%. The addition of Zr in the TX31 alloy did not change the type of second-phase particles, but the area fraction of white particles decreased to 2.1%. However, the area fraction of white particles in the TXZ311 alloy increased to 11.0% compared to the TX31 alloy. The same CaMgSn and Mg_2Cu phases were present in the TXCZ3111 alloy as in the TXC311 alloy, but the area fraction of white particles was slightly increased. In addition, the enrichment of Mg, Zn, and Cu was detected in the TXCZ3111 alloy. Based on previous research, this was inferred to be the MgZnCu phase [15].

Table 2. The phase area fraction and phase size distribution of six as-extruded alloys.

Alloy	Area Fraction of Second Phase (%)	Second-Phase Size Distribution (μm)			
		CaMgSn	Mg_2Sn	Mg_2Cu	MgZnCu
T3	2.5 ± 0.5%	-	5~70 μm	-	-
TX31	7.5 ± 1.0%	5~90 μm	-	-	-
TXK311	2.1 ± 0.6%	5~50 μm	-	-	-
TXZ311	11.0 ± 3.1%	10~200 μm	-	-	-
TXC311	8.0 ± 1.4%	58~110 μm	-	30~70 μm	-
TXCZ3111	9.1 ± 1.8%	5~100 μm	-	20~40 μm	20~30 μm

Table 3. EDS results of the as-extruded alloys.

Point	Chemical Composition (at.%)					Phase Types
	Mg	Sn	Ca	Zn	Cu	
A	75.74	24.26	-	-	-	Mg_2Sn
B	57.19	19.82	22.98	-	-	CaMgSn
C	91.24	4.70	4.07	-	-	CaMgSn
D	66.50	17.89	14.58	-	-	CaMgSn
E	72.87	-	-	-	27.13	Mg_2Cu
F	72.90	15.35	11.33	-	-	CaMgSn
G	94.81	2.83	2.36	-	-	CaMgSn
H	75.53	-	-	-	24.47	Mg_2Cu
I	65.36	-	-	16.92	17.72	MgZnCu

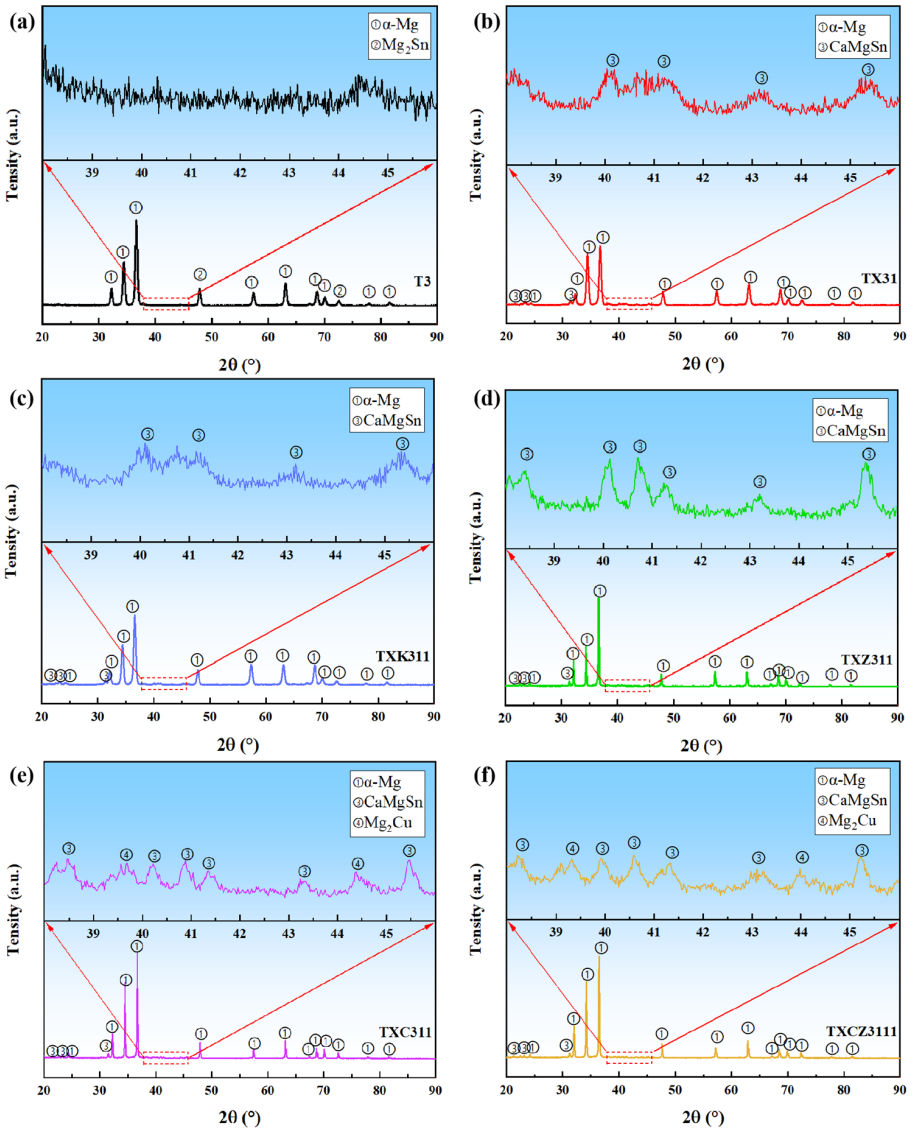


Figure 2. XRD patterns of six as-extruded alloys: (**a**) T3, (**b**) TX31, (**c**) TXK311, (**d**) TXZ311, (**e**) TXC311, and (**f**) TXCZ3111.

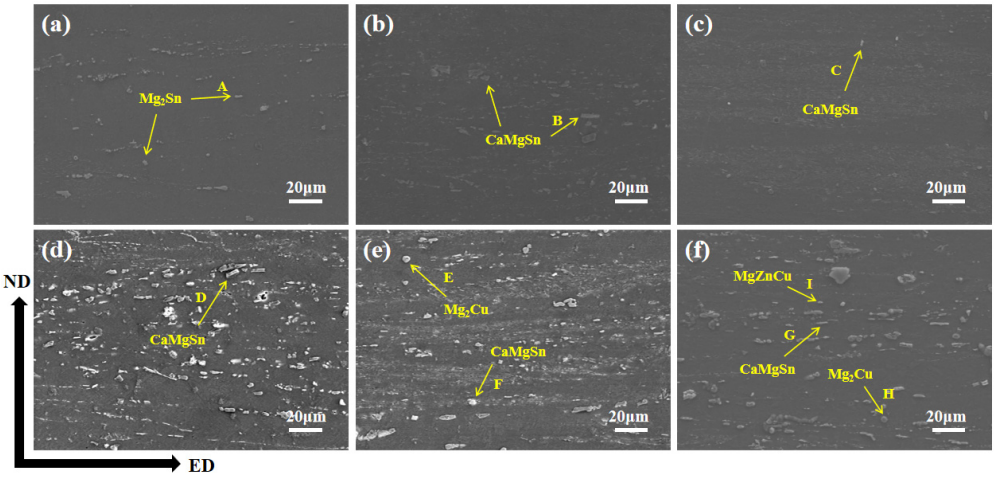


Figure 3. SEM images of six as-extruded alloys: (**a**) T3, (**b**) TX31, (**c**) TXK311, (**d**) TXZ311, (**e**) TXC311, and (**f**) TXCZ3111.

Figures 4 and 5 show the inverse pole figure maps, pole figures, and orientation angle distributions of the alloys. The grain sizes of the six alloys were 9.2 ± 1.3 μm, 3.5 ± 0.2 μm, 1.8 ± 0.2 μm, 5.1 ± 0.3 μm, 4.5 ± 0.5 μm, and 3.5 ± 0.5 μm. In this study, grain boundaries with misorientation angles greater than 10° were defined as high-angle grain boundaries (HAGBs). The HAGBs of the T3 alloy were 88.3%, and the texture intensity was 10.45. After adding Ca, the grain size exhibited a bimodal structure, the texture intensity was reduced to 6.64, and the HAGBs decreased to 69.3%. The average grain size of the TXK311 alloy was only 1.8 μm, the texture weakened, and the HAGBs increased to 90.3%. The HAGBs of the TXZ311 alloy, TXC311 alloy, and TXCZ3111 alloy were similar at 80.2%, 82.3%, and 79.5%, respectively. The texture intensity of the TXZ311 alloy increased to 16.85. The texture intensity of the matrix was not significantly affected by the addition of Cu or Cu/Zn.

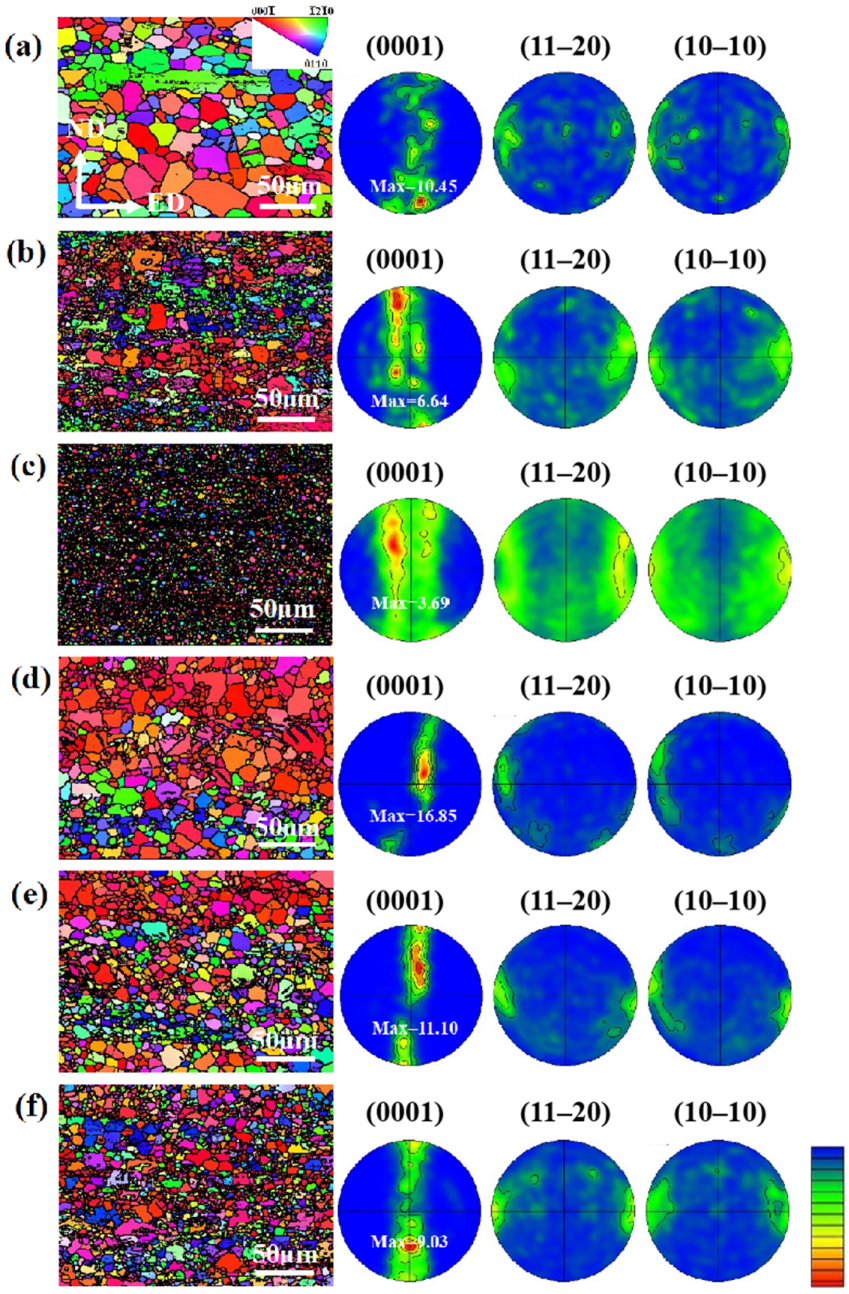


Figure 4. Inverse pole figure maps and pole figures: (**a**) T3, (**b**) TX31, (**c**) TXK311, (**d**) TXZ311, (**e**) TXC311, and (**f**) TXCZ3111.

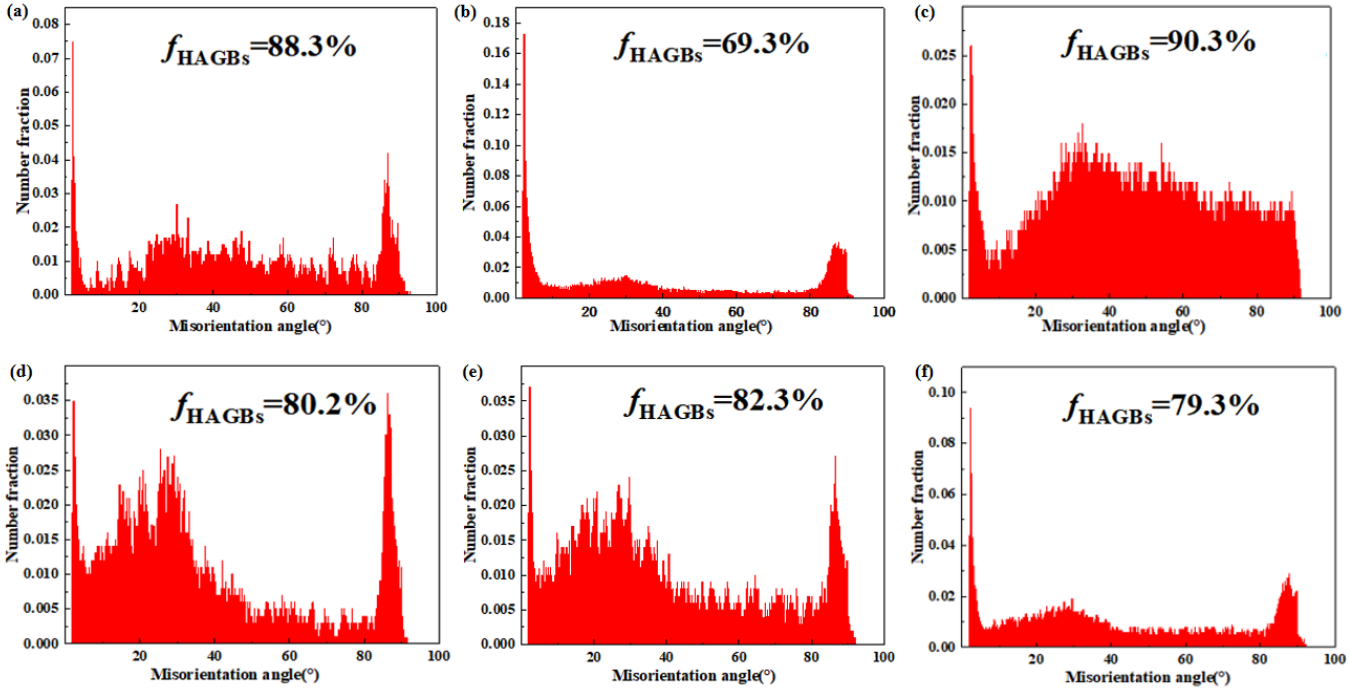


Figure 5. Misorientation angle area fraction distribution: (**a**) T3, (**b**) TX31, (**c**) TXK311, (**d**) TXZ311, (**e**) TXC311, and (**f**) TXCZ3111.

3.2. Electrochemical Behavior

Figure 6 illustrates the polarization curve. The E_{corr} obtained from the polarization curve represented a thermodynamic parameter, while i_{corr} served as a dynamic parameter that quantified the corrosion rate of materials. In practical applications, i_{corr} was mainly intended to characterize the corrosion properties of materials. The fitting values of E_{corr} and i_{corr} in Figure 6 are indicated in Table 4. The alloys were ranked in terms of corrosion current density as follows: TXZ311 < TXK311 < T3 < TX31 < TXCZ3111 < TXC311. According to Equation (2), the TXZ311 alloy had the lowest corrosion rate. Obvious breakdown points of the passive film were detected on the anode curves of the TXC311 and TXCZ3111 alloys. When the voltage surpassed the breakdown potential, the self-corrosion current density of both alloys increased significantly. Generally, the more positive the voltage at which the alloy reached the breakdown potential, the slower the increase in the self-corrosion current density. Accordingly, the increase in the self-corrosion current density for the TXCZ3111 alloy was slower than that of the TXC311 alloy, indicating that the passive film on the TXCZ3111 alloy exhibited better corrosion resistance. However, once the breakdown potential was exceeded, cracks formed in the corrosion product films on both alloys, leading to a substantial increase in their self-corrosion current densities. This implied that the passive film had broken down, which would have hastened the corrosion of the alloy [16].

Table 4. Fitting parameters from polarization curves of six as-extruded alloys.

Alloy	E_{corr} (V)	i_{corr} (μA·cm^{-2})	P_i (mm·year^{-1})
T3	−1.54	58.40	1.33
TX31	−1.50	63.30	1.45
TXK311	−1.46	50.60	1.16
TXZ311	−1.45	31.50	0.72
TXC311	−1.48	91.90	2.10
TXCZ3111	−1.45	71.90	1.64

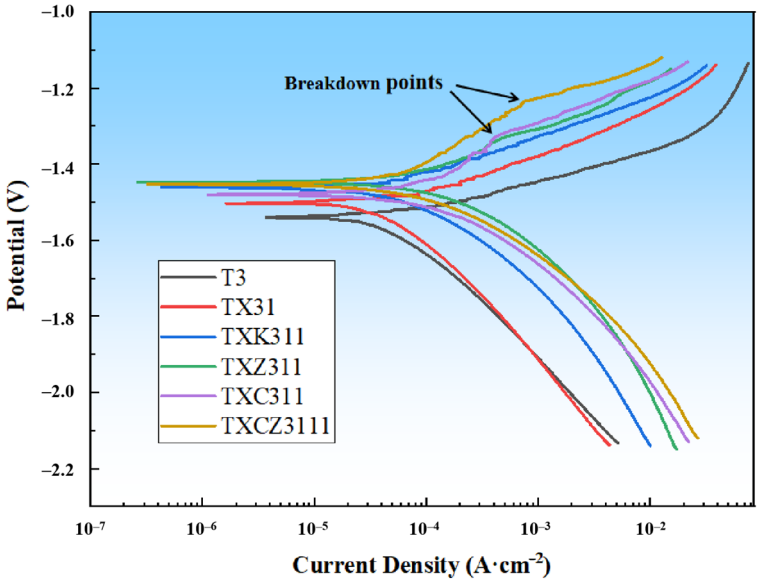


Figure 6. The potentiodynamic polarization curves of six as-extruded alloys in 3.5 wt.% NaCl solution.

Figure 7 shows the electrochemical impedance spectrum (EIS) of the as-extruded alloys. The low-frequency impedance modulus was commonly used to estimate the anti-corrosion capacity of Mg alloys [17,18]. The Bode diagram in Figure 7a,b indicates the following rank of corrosion resistance for alloys: TXZ311 > TXK311 > T3 > TX31 > TXCZ3111 > TXC311. Figure 7c illustrates the Nyquist images of the as-extruded alloys. According to the literature [19,20], the T3, TX31, TXK311, and TXZ311 alloys were fitted by the circuit in Figure 7d, while the TXC311 and TXCZ3111 alloys were fitted by the circuit in Figure 7e. The solution resistance is denoted by R_s, CPE_{dl} represents the bilayer capacity, and R_f and CPE_f refer to the corrosion film layer resistance and capacitance, respectively, and they were used to describe low-frequency capacitor circuits. The charge transfer resistance in solution is expressed as R_{ct}, and the partial oxide film breakage is indicated by R_L and L. The fitting values are listed in Table 5. The EIS results provided further insights into the electrochemical corrosion behavior of the alloys. The charge transfer resistance (Rct) of the TXZ311 alloy was significantly higher than that of the other alloys, indicating a lower dissolution rate when the solution contacted the alloy through the pores of the surface film. This suggested that the oxide layer on the surface of the TXZ311 alloy provided effective protection, thereby mitigating corrosion. Additionally, this result indicated that the micro-galvanic corrosion caused by the second phase acting as a cathode was relatively weak. The CPEdl represented the double-layer capacitance at the interface between the alloy surface and the electrolyte. The lower CPEdl value of the TXZ311 alloy reflected a smaller localized corrosion area, which further contributed to delaying the corrosion of the alloy. The corrosion resistance of the six alloys was evaluated by Rct, and the order was as follows: TXZ311 > TXK311 > T3 > TX31 > TXCZ3111 > TXC311.

Table 5. Fitting electrochemical parameters from the EIS measurement of six as-extruded alloys.

Alloy	R_s	CPE_{dl}		R_{ct}	CPE_f		R_f	R_2	L
	$\Omega \cdot cm^2$	$Y_1/\mu\Omega^{-1} \cdot cm^{-2}$	n_1	$\Omega \cdot cm^2$	$Y_2/\mu\Omega^{-1} \cdot cm^{-2}$	n_2	$\Omega \cdot cm^2$	$\Omega \cdot cm^2$	$H \cdot cm^2$
T3	0.36 ± 0.03	32.42 ± 1.23	0.96	37.51 ± 2.36	-	-	-	186.1 ± 10.3	339.7 ± 19.2
TX31	0.37 ± 0.02	51.26 ± 2.26	0.91	26.53 ± 1.49	-	-	-	136.7 ± 9.5	288.6 ± 16.3
TXK311	3.29 ± 0.13	106.10 ± 3.26	0.84	57.17 ± 2.26	-	-	-	198.5 ± 16.6	583.4 ± 18.2
TXZ311	4.979 ± 0.16	47.20 ± 1.05	0.88	65.94 ± 3.36	-	-	-	228.8 ± 12.5	631.2 ± 26.3
TXC311	2.629 ± 0.14	0.70 ± 0.02	0.91	3.958 ± 0.24	4.653 ± 0.34	0.92	32.77 ± 1.34	38.4 ± 2.3	110.0 ± 10.3
TXCZ3111	2.58 ± 0.08	205.2 ± 1.25	0.91	19.17 ± 2.27	3.387 ± 0.46	0.81	4.185 ± 0.86	21.21 ± 1.4	143.5 ± 6.5

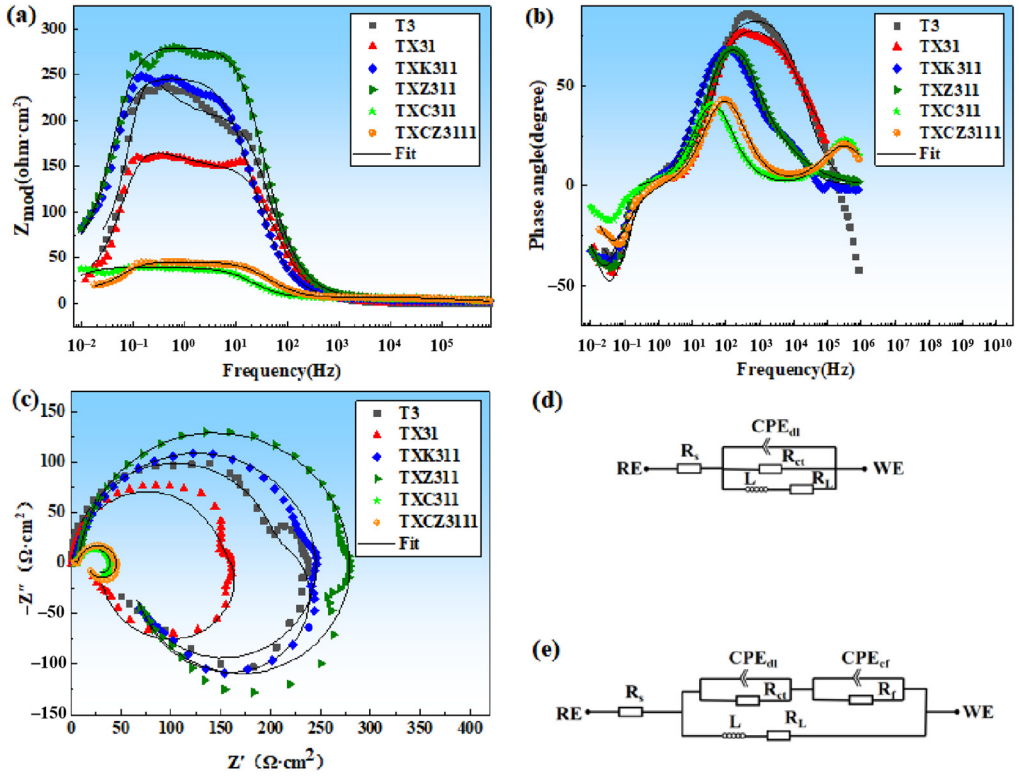


Figure 7. The EIS plots of six as-extruded alloys: (**a**) Bode diagram, (**b**) phase angle diagram, (**c**) Nyquist curves, and (**d**,**e**) equivalent circuit diagram.

3.3. Immersion Test

Figure 8 depicts the H_2 evolution volume and the average corrosion rate. In Figure 8a, the H_2 evolution volume of the T3, TX31, TXK311, and TXZ311 alloys slowed down after immersing for 12 h, while the H_2 precipitation volumes of the TXC311 and TXCZ3111 alloys remained relatively stable. As depicted in Figure 8b, the order of corrosion rates was TXZ311 < TXK311 < T3 < TX31 < TXCZ3111 < TXC311, which was consistent with the results of EIS.

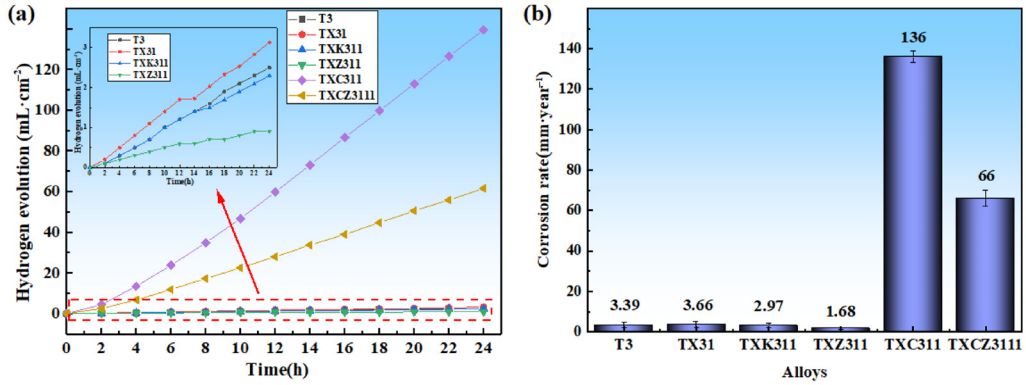


Figure 8. (**a**) H_2 evolution volume; (**b**) corrosion rate.

Figure 9 presents the surface macroscopic and SEM images of the alloy that had been immersed for 24 h to remove corrosion products. The macroscopic image revealed that the as-extruded alloy exhibited corrosion marks along the extrusion direction. Among these, the TXZ311 alloy was the least corroded, whereas the TXC311 alloy was the most severely corroded. The surfaces of the six alloys exhibited pits of varying depths of corrosion. Due to the inhomogeneity in the grain structure, many localized deep pits were observed in

the ED direction of the TX31 alloy. In contrast, the corrosion process had been relatively uniform for the T3 and TXK311 alloys, whereas localized corrosion pits were only found in the TXZ311 alloy. Deeper lamellar corrosion pits had been observed in the TXC311 and TXCZ3111 alloys, which exhibited the most severe corrosion. These findings indicated that the TXZ311 alloy exhibited superior corrosion resistance.

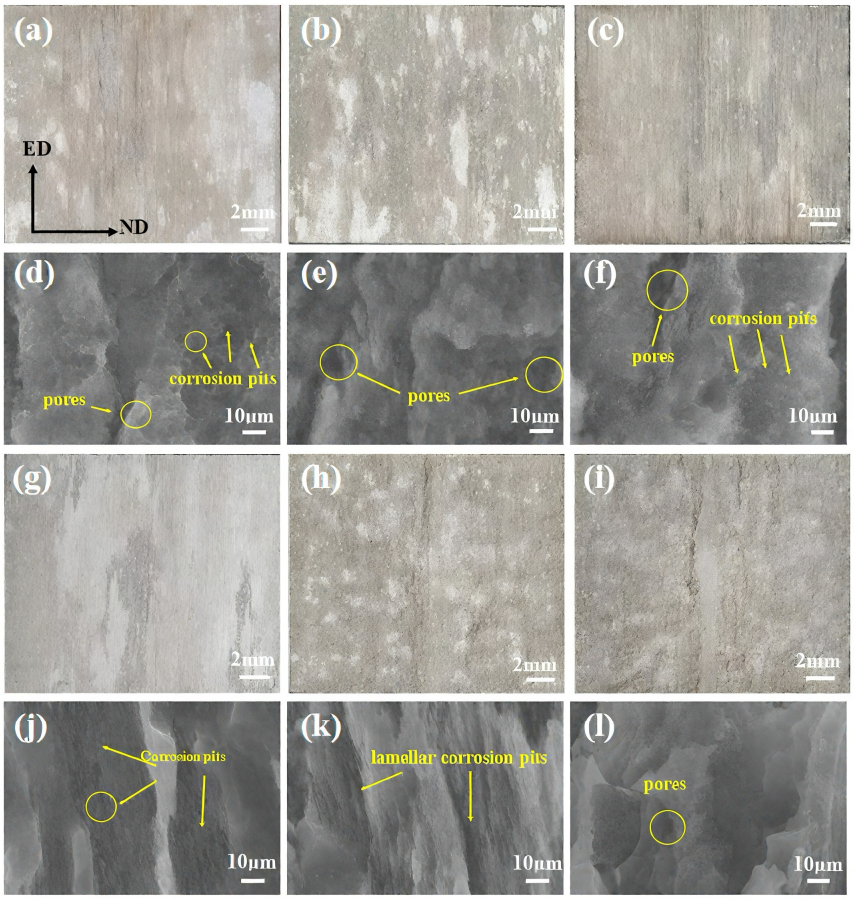


Figure 9. Macroscopic and SEM images: (**a**,**d**) T3, (**b**,**e**) TX31, (**c**,**f**) TXK311, (**g**,**j**) TXZ311, (**h**,**k**) TXC311, and (**i**,**l**) TXCZ3111.

The SEM/EDS analysis of the uncleared corrosion products after 24 h of alloy corrosion is presented in Figure 10. The surfaces of all alloys were covered with spherical corrosion products of varying thicknesses. In comparison, it was found that the corrosion products formed by the T3, TXK311, and TXZ311 alloys were thicker and more evenly distributed, indicating good adhesion to the Mg matrix and the potential to prevent further Cl^- corrosion. Conversely, the products on the TX31, TXC311, and TXCZ3111 alloy surfaces did not fully cover the surface. Large corrosion cracks and alloy exposure were observed, attributed to the relatively loose corrosion products that gradually detached during immersion, providing limited protection to the matrix. These results indicate that Zr and Zn positively impacted the corrosion resistance of the TX31 alloy by forming a denser corrosion product film.

The XPS analysis was conducted to compare the surface film composition of the TXZ311 alloy in air and solution, as illustrated in Figure 11. As shown in Figure 11a, diffraction peaks of Mg, Sn, Ca, Zn, and O were present on the alloy surface in both conditions. Figure 11b–f indicate that the oxide film formed in dry air was primarily composed of MgO, CaO, $CaCO_3$, and ZnO. Figure 11g–k demonstrate that the product film after immersion in a 3.5 wt.% NaCl solution consisted of $Mg(OH)_2$, SnO_2, $Ca(OH)_2$, and ZnO.

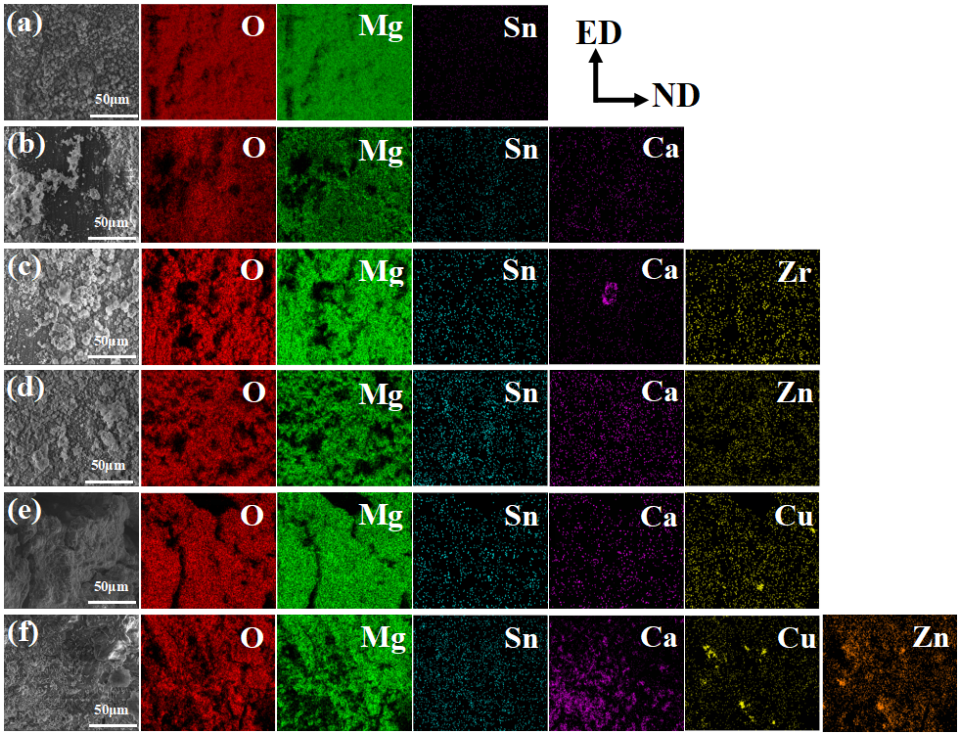


Figure 10. SEM/EDS plots of the corrosion product film: (**a**) T3, (**b**) TX31, (**c**) TXK311, (**d**) TXZ311, (**e**) TXC311, and (**f**) TXCZ3111.

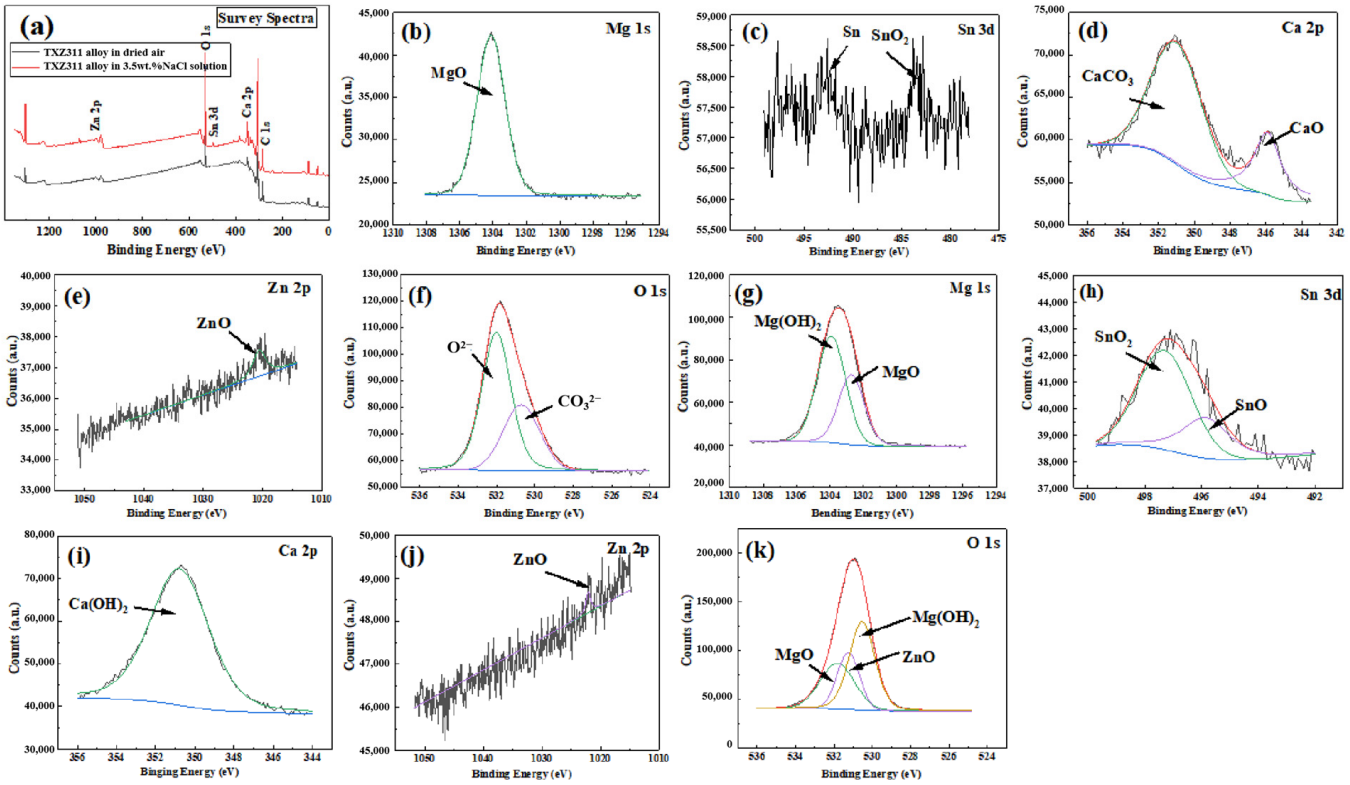


Figure 11. XPS analysis of the TXZ311 alloy: (**a**) survey spectrum, (**b**–**f**) binding energy of Mg 1s, Sn 3d, Ca 2p, Zn2p, and O 1s in dry air, respectively, and (**g**–**k**) binding energy of Mg 1s, Sn 3d, Ca 2p, Zn2p, and O 1s in 3.5wt.%NaCl solution, respectively.

Figure 12 illustrates the SEM and a partially enlarged view of the vertical section of the alloys after 24 h of immersion. The corrosion depth of the T3 alloy was 18 ± 2 μm, and white particles were detected near the cracks, hindering their extension. Based on the XRD and EDS results presented in the previous sections, it was speculated that these white secondary phases were the Mg_2Sn phase. The cross section of the corrosion pit was extracted and observed using SEM. The depth of the corrosion pits was measured using Image-Pro Plus v6.0 software. The corrosion depth of the TX31 alloy was 51 ± 5 μm, and the crack was deep. The corrosion depth of the TXK311 alloy was 15 ± 1 μm, with many fine white particles observed at the crack. Based on previous XRD and EDS studies, it was speculated that the white secondary phases were the CaMgSn phase. The corrosion depth of the TXZ311 alloy was only 12 ± 1 μm, with fewer cracks observed. In contrast, the TXC311 and TXCZ3111 alloys were severely corroded, with corrosion depths of 210 ± 5 μm and 138 ± 7 μm, respectively. The corrosion surfaces of the T3 and TX31 alloys were relatively uniform, with fewer cracks observed; however, localized corrosion pits were present, particularly in the TX31 alloy, where the cracks were deeper. In contrast, the TXK311 and TXZ311 alloys displayed smoother and more compact corrosion surfaces, with significantly fewer cracks and shallower pits, reflecting a more uniform corrosion process. The TXC311 and TXCZ3111 alloys exhibited the most severe corrosion damage, with extensive cracks visible across the surface, indicating a rougher and more fragmented morphology compared to the other alloys.

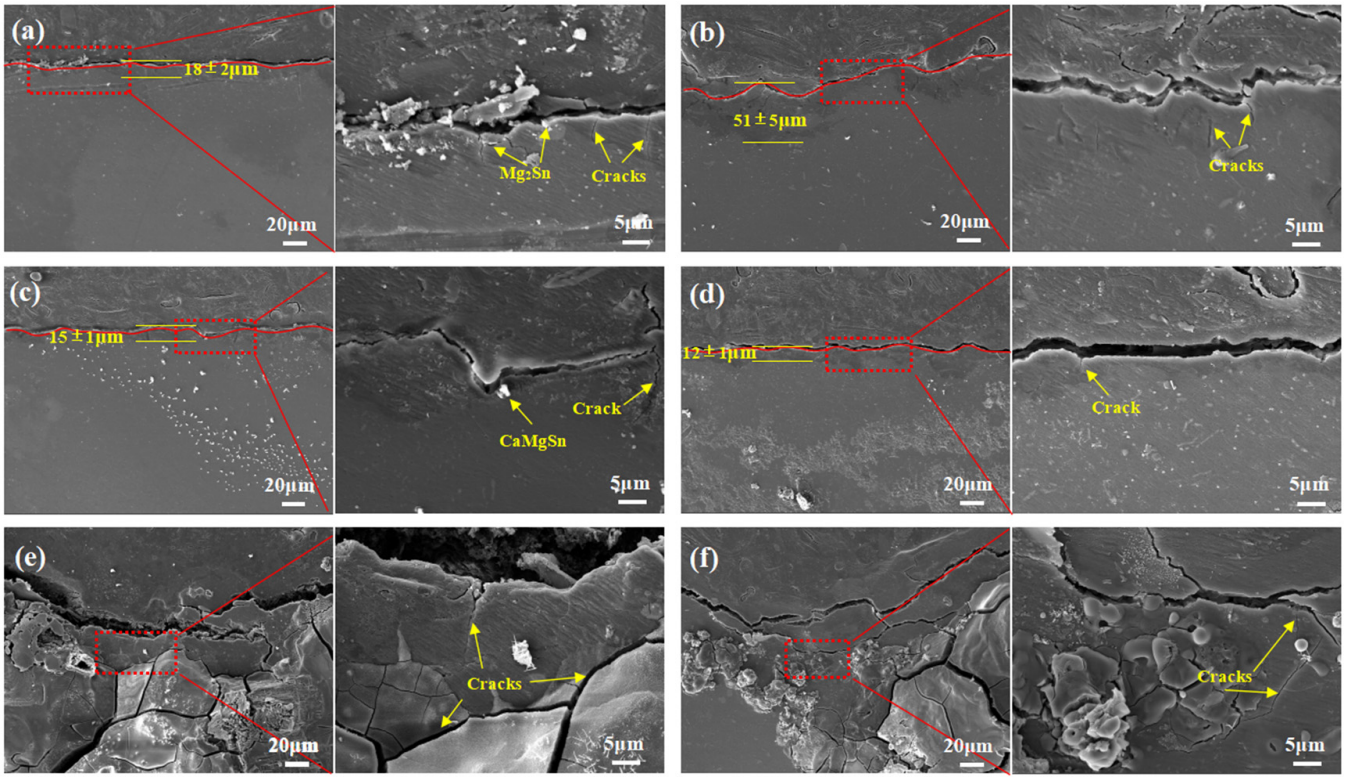


Figure 12. Longitudinal section corrosion morphology and local enlarged view of six as-extruded alloys: (**a**) T3, (**b**) TX31, (**c**) TXK311, (**d**) TXZ311, (**e**) TXC311, and (**f**) TXCZ3111.

4. Discussion

4.1. Effect of Grain Size and Second Phase on Corrosion Behavior

The corrosion rate of Mg alloys was significantly influenced by the grain size, phase structure, and distribution resulting from extrusion and deformation processes [21–24]. Numerous investigations [25–28] have demonstrated that a finer grain size can reduce the

corrosion experienced by the alloy. Ralston [29] demonstrated that the relationship between the corrosion rate (i_{corr}) and grain size (d) is described by Equation (3):

$$i_{corr} = A + Bd^{-0.5} \quad (3)$$

where A and B denote constants. The grain size influences the conductivity of the oxide film by altering the grain boundary density. When the Mg alloy corrodes to form a stable corrosion product, constant B is negative, indicating that the Mg alloy will be protected. Conversely, when constant B is positive, a smaller grain size increases the conductivity of the oxide film, which reduces the corrosion resistance of the alloy.

On the corrosion surface of the TX31 alloy, the grain distribution was not uniform, with smaller grain regions exhibiting higher grain boundary density. Grain boundaries acted as local electrodes, accelerating the localized corrosion of the Mg matrix. This phenomenon explains why the TX31 alloy produced large corrosion pits locally.

The corrosion rate is influenced by the types and amounts of precipitated phases in Mg alloys [30]. In a corrosive medium, electrochemical corrosion typically occurs between the precipitated phases, which act as micro-cathodes, and the Mg matrix. This interaction leads to rapid corrosion in the vicinity of the precipitated phases [31]. When the precipitated phases have a larger area and are more evenly distributed, a denser film of corrosion products forms on the Mg matrix, serving as a barrier to mitigate corrosion [32].

The corrosion properties of the six alloys were ranked as follows: TXZ311 > TXK311 > T3 > TX31 > TXCZ3111 > TXC311. The addition of Ca and Cu increased the corrosion rates of the T3 and TX31 alloys, respectively. The corrosion rate of the TX31 alloy was significantly reduced by the addition of Zn and Zr. In the T3 alloy, the white phase area fraction was only 2.5%; therefore, less galvanic corrosion occurred. From the longitudinal section corrosion morphology in Figure 12a, it was observed that the Mg_2Sn phase hindered the deepening of corrosion. The white phase area of the TX31 alloy increased by 7.5% compared to the T3 alloy. In the TX31 alloy, the increase in the CaMgSn phase caused elevated galvanic corrosion, and no obvious white phases were found in the longitudinal section corrosion cracks shown in Figure 12b. After adding Zr, the grain size and area fraction of the second phase of the TX31 alloy decreased to the lowest values, 1.8 μm and 2.1%, respectively. The corrosion performance of the TXK311 alloy was enhanced due to the refined grain size and the decreased area fraction of the white phase. As demonstrated in Figure 12c, the fine CaMgSn phase hindered the deepening of the erosion crack. The TXC311 and TXCZ3111 alloys were the most severely corroded due to the higher potential of the Mg_2Cu phase (−1.69), which caused α-Mg and the Mg_2Cu phase to create micro-galvanic corrosion, reducing the alloy's resistance to corrosion [33]. In the TXCZ3111 alloy, a small percentage of the produced MgZnCu phase consumed the Mg_2Cu phase, thereby improving the corrosion resistance of the alloy [34].

4.2. Effect of Texture on Corrosion Performance

Upon the immersion of Mg alloys in a corrosive solution, an unstable Mg oxide is formed, allowing Cl^- and H_2O molecules to penetrate the metal. Due to the structural discontinuity between the Mg matrix and the oxide film, tensile stress occurs in the oxide films [32]. Tensile stress accelerates the breakdown of MgO when the adherence of the corrosion product layer in the corrosive medium is poor. Cui [24] and Argade et al. [35] proposed that a higher fraction of HAGBs enhances the corrosion resistance of the alloy in corrosive media. The introduction of HAGBs results in reduced tensile stress [36]. As shown in Figure 5, the ratio of HAGBs in as-extruded alloys was TXK311 > T3 > TXC311 > TXZ311 > TXCZ3111 > TX31. Nevertheless, the reduction in tensile stress depends on the development of a stabilized oxide layer in a passivating atmosphere. The surface product film of the TXC311 and TXCZ3111 alloys could not cover the alloy surface completely. Therefore, even with high HAGBs, a high corrosion rate persisted. The fraction of HAGBs in the TX31 alloy was the lowest, and the grain size was extremely uneven. According to Wang et al. [37], non-uniform grain sizes in as-extruded alloys result in higher corrosion

rates due to increased galvanic corrosion and non-uniform corrosion product films. In contrast, the HAGBs fraction of the TXZ311 and TXK311 alloys was 88.3% and 90.3%, respectively, resulting in better corrosion resistance.

The corrosion rate of Mg alloys has been reported to be influenced by crystal orientation [38–41]. For Mg, the (0001) plane has the highest atomic density [42,43]. Because this tightly packed plane has more atomic coordination, it exhibits lower surface energy. Atoms dissolve more slowly on surfaces with lower surface energy. As a result, the (0001) plane experiences the lowest corrosion rate of all Mg planes. Thus, efforts to reduce the corrosion rate of Mg alloys may focus on enhancing the texture intensity of the (0001) plane. Luo et al. [23] investigated as-extruded Mg-6Gd-2Y-0.2Zr alloys and revealed that the (11–20) and (10–10) planes were more susceptible to corrosion than the (0001) planes. Subsequently, Wang [37] and Song et al. [43] reported similar findings. Dobkowska et al. [21] described in their analysis that the (0001) planes in the Mg-4Li-3Al-1Zn alloy exhibit higher electrochemical stability. According to Figure 4, the texture intensity of the T3 and TXZ311 alloys is more intense, especially with the texture intensity of the TXZ311 reaching 16.85. Therefore, the TXZ311 alloy demonstrates enhanced corrosion performance.

4.3. Effect of Product Film on Corrosion Behavior

As previously analyzed, the product film formed on the TX31 alloy was loose, which did not effectively protect the Mg matrix. This was attributed to the presence of bimodal grains. In contrast, the TXZ311 alloy exhibited a higher fraction of HAGBs and a higher second-phase area fraction, resulting in more evenly distributed surface corrosion products. Combined with EDS and XPS analysis (Table 3 and Figure 11), it was found that the surface film of the TXZ311 alloy was primarily composed of $Mg(OH)_2$, SnO_2, ZnO, and $Ca(OH)_2$.

The stress state in the oxide film is described by the Pilling–Bedworth Ratio (PBR) [44,45]. The PBR indicates the volume ratio of ions/atoms on the surface of the material. When $1 < PBR < 2$, the oxide film is subjected to compressive stress, resulting in a denser film that protects the metal matrix. However, when $PBR < 1$ or $PBR > 2$, the product film fractures due to tensile stress, further exacerbating the corrosion of the metal. The calculated PBR values of the TXZ311 alloy product film are listed in Table 6. Comparing the PBR of the various products reveals that $Mg(OH)_2$ provides a protective effect on the Mg matrix in the initial phase. However, with prolonged immersion, Cl^- in the solution gradually dissolves the $Mg(OH)_2$ forming $MgCl_2$, thereby decreasing the corrosion resistance of Mg [46,47]. Unlike other alloys, the corrosion film layer in the TXZ311 alloy produces ZnO (with a PBR value of 1.59), which fills the pores of $Mg(OH)_2$, enhancing the film's compactness and reducing the contact between the alloy surface and the solution. This factor also contributes to the reduced corrosion rate of the TXCZ3111 alloy. The mechanism is illustrated in Figure 13.

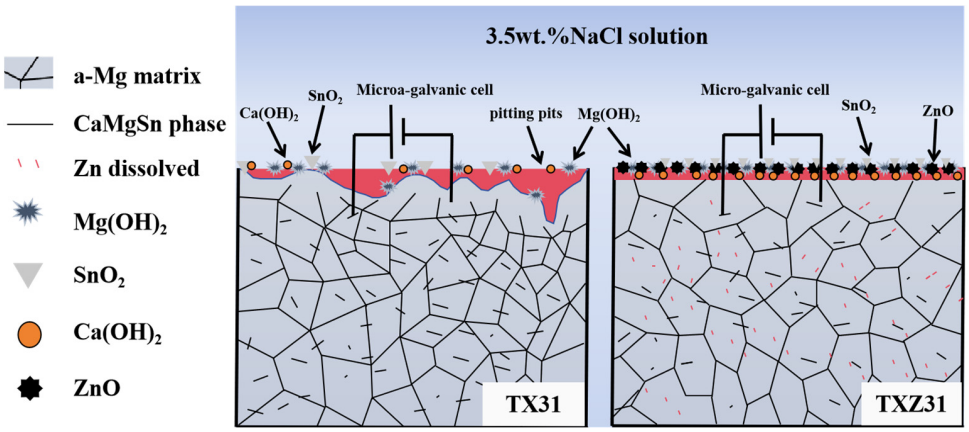


Figure 13. Corrosion schematic model of the TX31 and TXZ311 alloys.

Table 6. PBR compounds.

Compound	MgO	$Mg(OH)_2$	SnO_2	$Ca(OH)_2$	ZnO
PBR	0.8	1.8	1.3	1.3	1.59

Figure 14 summarizes the available data on the average corrosion rate of the Mg-Sn-Ca system Mg alloy in a 3.5 wt.% NaCl solution. The Mg-Sn-Ca system alloy is a crucial heat-resistant Mg alloy for applications; however, most current research has focused on mechanical properties rather than corrosion resistance. Consequently, the TXZ311 alloy proposed in this study exhibits a significantly lower corrosion rate compared to other Mg-Sn-Ca series alloys, potentially serving as a theoretical foundation for further applications of Mg-Sn-Ca alloys.

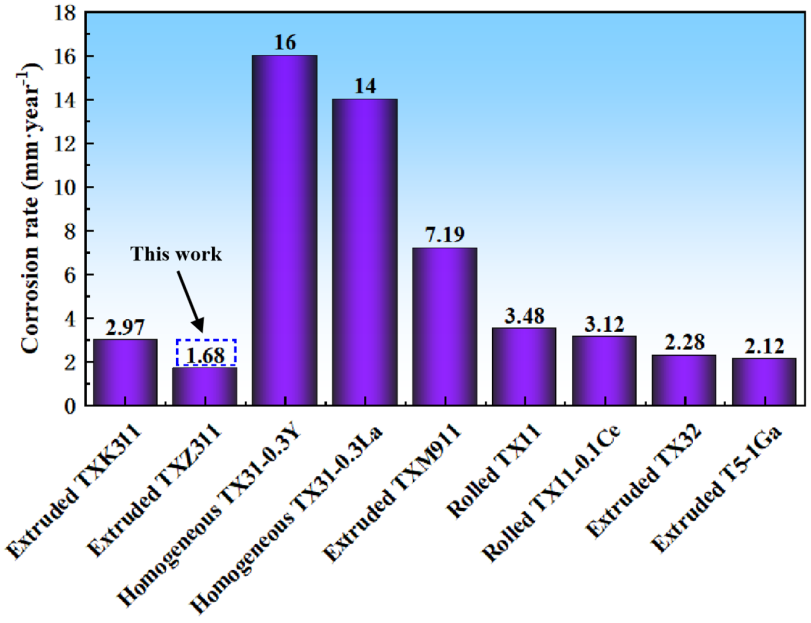


Figure 14. Corrosion rates of Mg-Sn-Ca alloys [7,48–51].

5. Conclusions

The effects of the grain size, second phase, corrosion product film, and texture intensity on the corrosion properties were investigated. The main results are as follows:

(1) The addition of Zr and Zn did not alter the phase composition of the TX31 alloy but changed the area fraction of the second phase. However, the introduction of Cu led to the formation of a new Mg_2Cu phase. Among these alloys, the TXZ311 alloy exhibited the highest area fraction of the second phase, while the TXK311 alloy had the lowest.

(2) The TXZ311 alloy exhibited the best corrosion resistance, with a corrosion rate of only 1.68 mm·year^{-1}. This alloy had a higher HAGBs fraction and greater matrix texture intensity. The formation of ZnO within the corrosion product film of the TXZ311 alloy filled the voids created by $Mg(OH)_2$, thereby enhancing the film's stability. The synergistic effect of these factors contributed significantly to the improved corrosion resistance of the TXZ311 Mg alloy.

(3) The TXK311 alloy showed superior corrosion resistance due to its uniform and fine grain size as well as a high fraction of HAGBs. In contrast, the bimodal structure of the TX31 alloy resulted in inferior corrosion resistance, and the uneven grain size led to significant localized corrosion.

(4) The addition of Cu resulted in the formation of a new Mg_2Cu phase, which has a relatively high electrode potential (−1.69 V). This led to micro-galvanic corrosion between the α-Mg and Mg_2Cu phases, thereby reducing the corrosion resistance of the TXC311 and TXCZ3111 alloys.

Author Contributions: Conceptualization, Z.J. and S.D.; methodology, Z.J.; software, X.N.; validation, Z.J., S.D. and X.N.; formal analysis, X.N.; investigation, S.D.; resources, Z.J.; data curation, X.N.; writing—original draft preparation, S.D.; writing—review and editing, Z.J. and X.N.; visualization, X.N.; supervision, Z.J.; project administration, Z.J.; funding acquisition, Z.J. All authors have read and agreed to the published version of the manuscript.

Funding: This research was funded by the National College Students' Entrepreneurship Project (202311035033); the Liaoning Province Natural Science Foundation Project of China (2023-MS-321); and the Liaoning Province International Cooperation Project (Project Number: 2023030491-JH2/107).

Data Availability Statement: If needed, the corresponding author can provide access to the datasets generated and/or analyzed during the current study upon request that is deemed reasonable.

Acknowledgments: The authors acknowledge the National College Students' Entrepreneurship Project (202311035033); the financial support from the Liaoning Province Natural Science Foundation Project of China (2023-MS-321); and the Liaoning Province International Cooperation Project (Project Number: 2023030491-JH2/107).

Conflicts of Interest: The authors declare no conflict of interest.

References

1. Dvorsky, D.; Kubasek, J.; Vojtech, D.; Minarik, P. Novel aircraft Mg-Y-Gd-Ca alloys with high ignition temperature and suppressed flammability. *Mater. Lett.* **2020**, *264*, 127313. [CrossRef]
2. Wan, D.; Xue, Y.; Hu, J.; Wang, H.; Liu, W. Corrosion and chemical behavior of Mg 97 Zn 1 Y 2-1wt.% SiC under different corrosion solutions. *China Foundry* **2021**, *18*, 68–74. [CrossRef]
3. Farhadi, S.S.; Aliofkhazraei, M.; Darband, G.B.; Abolhasani, A.; Rouhaghdam, A.S. Corrosion and wettability of PEO coatings on magnesium by addition of potassium stearate. *J. Magnes. Alloys* **2017**, *5*, 210–216. [CrossRef]
4. Jiang, X.; Guo, R.G.; Jiang, S.Q. Evaluation of self-healing ability of Ce-V conversion coating on AZ31 magnesium alloy. *J. Magnes. Alloys* **2016**, *4*, 230–241. [CrossRef]
5. Guo, L.; Wu, W.; Zhou, Y.; Zhang, F.; Zeng, R.; Zeng, J. Layered double hydroxide coatings on magnesium alloys: A review. *J. Mater. Sci. Technol.* **2018**, *34*, 1455–1466. [CrossRef]
6. Fu, Y.; Liu, C.; Hao, H.; Xu, Y.; Zhu, X. Effect of ageing treatment on microstructures, mechanical properties and corrosion behavior of Mg-Zn-RE-Zr alloy micro-alloyed with Ca and Sr. *China Foundry* **2021**, *18*, 131–140. [CrossRef]
7. Abu Leil, T.; Hort, N.; Dietzel, W.; Blawert, C.; Huang, Y.; Kainer, K.U.; Rao, K.P. Microstructure and corrosion behavior of Mg-Sn-Ca alloys after extrusion. *Trans. Nonferrous Met. Soc. China* **2009**, *19*, 40–44. [CrossRef]
8. Chang, L.L.; Tang, H.; Guo, J. Strengthening effect of nano and micro-sized precipitates in the hot-extruded Mg-5Sn-3Zn alloys with Ca addition. *J. Alloys Compd.* **2017**, *703*, 552–559. [CrossRef]
9. Wan, D.; Sun, Y.; Xue, Y.; Dong, S.; Han, G.; Wang, Y.; Yang, F.; Tang, H.; Wang, Y. Improvement in corrosion resistance of $Mg_{97}Zn_1Y_2$ alloy by Zr addition. *China Foundry* **2024**, 1–7. [CrossRef]
10. Wang, S.D.; Xu, D.K.; Wang, B.J.; Sheng, L.Y.; Qiao, Y.X.; Han, E.-H.; Dong, C. Influence of phase dissolution and hydrogen absorption on the stress corrosion cracking behavior of Mg-7%Gd-5%Y-1%Nd-0.5%Zr alloy in 3.5 wt.% NaCl solution. *Corros. Sci.* **2018**, *142*, 185–200. [CrossRef]
11. Yin, S.Q.; Duan, W.C.; Liu, W.H.; Wu, L.; Yu, J.M.; Zhao, Z.L.; Liu, M.; Wang, P.; Cui, J.; Zhang, Z.Q. Influence of specific second phases on corrosion behaviors of Mg-Zn-Gd-Zr alloys. *Corros. Sci.* **2020**, *166*, 108419. [CrossRef]
12. Ha, H.Y.; Kang, J.Y.; Yang, J.; Yim, C.D.; You, B.S. Limitations in the use of the potentiodynamic polarisation curves to investigate the effect of Zn on the corrosion behaviour of as-extruded Mg-Zn binary alloy. *Corros. Sci.* **2013**, *75*, 426–433. [CrossRef]
13. Lotfpour, M.; Emamy, M.; Dehghanian, C.; Tavighi, K. Influence of Cu addition on the structure, mechanical and corrosion properties of cast Mg-2%Zn alloy. *J. Mater. Eng. Perform.* **2017**, *26*, 2136–2150. [CrossRef]
14. Shi, Z.; Atrens, A. An innovative specimen configuration for the study of Mg corrosion. *Corros. Sci.* **2011**, *53*, 226–246. [CrossRef]
15. Wang, C.M.; Guo, S.; Zeng, L.M.; Zheng, D.S.; Xu, J.C.; Yang, M.N.; Liang, T.X. Effects of second phases on microstructure, microhardness, and corrosion behavior of Mg-3Sn-(1Ca) alloys. *Materials* **2019**, *12*, 2515. [CrossRef]
16. Zhao, M.C.; Liu, M.; Song, G.L.; Atrens, A. Influence of pH and chloride ion concentration on the corrosion of Mg alloy ZE41. *Corros. Sci.* **2008**, *50*, 3168–3178. [CrossRef]
17. Wu, G.S.; Zhang, X.M.; Zhao, Y.; Ibrahim, J.M.; Yuan, G.Y.; Chu, P.K. Plasma modified Mg-Nd-Zn-Zr alloy with enhanced surface corrosion resistance. *Corros. Sci.* **2014**, *78*, 121–129. [CrossRef]
18. Wu, H.; Xiao, S.; Chen, D.; Qasim, A.M.; Ding, K.; Wu, G.; Chu, P.K. Effects of diamond like carbon film on the corrosion behavior of NdFeB permanent magnet. *Surf. Coat. Technol.* **2017**, *312*, 66–74. [CrossRef]
19. Yang, L.Z.; Feng, Y.; He, Y.Q.; Yang, L.Y.; Liu, H.C.; Wang, X.F.; Peng, C.Q.; Wang, R.C. Effect of Sc/Sm microalloying on microstructural and properties of Mg-2Zn-0.3Ca biodegradable alloy. *J. Alloys Compd.* **2022**, *907*, 164533. [CrossRef]

20. Yamasaki, M.; Shi, Z.; Atrens, A.; Furukawa, A.; Kawamura, Y. Influence of crystallographic orientation and Al alloying on the corrosion behaviour of extruded α-Mg/LPSO two-phase Mg-Zn-Y alloys with multimodal microstructure. *Corros. Sci.* **2022**, *200*, 110237. [CrossRef]
21. Dobkowska, A.; Cieślak, B.A.; Kuc, D.; Hadasik, E.; Płociński, T.; Ura-Bińczyk, E.; Mizera, J. Influence of bimodal grain size distribution on the corrosion resistance of Mg-4Li-3Al-1Zn (LAZ431). *J. Mater. Res. Technol.* **2021**, *13*, 346–358. [CrossRef]
22. Wan, Y.; Xu, S.; Liu, C.; Gao, Y.; Jiang, S.; Chen, Z. Enhanced strength and corrosion resistance of Mg-Gd-Y-Zr alloy with ultrafine grains. *Mater. Lett.* **2018**, *213*, 274–277. [CrossRef]
23. Luo, Y.F.; Deng, Y.L.; Guan, L.Q.; Ye, L.Y.; Guo, X.B.; Luo, A. Effect of grain size and crystal orientation on the corrosion behavior of as-extruded Mg-6Gd-2Y-0.2Zr alloy. *Corros. Sci.* **2020**, *164*, 108338. [CrossRef]
24. Cui, Q.; Yi, D.Q.; Wang, H.X.; Zhang, J.Y.; Xu, J.; Wang, B. Effects of grain size and secondary phase on corrosion behavior and electrochemical performance of Mg-3Al-5Pb-1Ga-Y sacrificial anode. *J. Rare Earths* **2019**, *37*, 1341–1350. [CrossRef]
25. Fang, X.W.; Yang, J.N.; Wang, S.P.; Wang, C.B.; Huang, K.; Li, H.N.; Lu, B.H. Additive manufacturing of high performance AZ31 magnesium alloy with full equiaxed grains: Microstructure, mechanical property, and electromechanical corrosion performance. *J. Mater. Process. Technol.* **2022**, *300*, 117430. [CrossRef]
26. Patel, V.; Li, W.Y.; Andersson, J.; Li, N. Enhancing grain refinement and corrosion behavior in AZ31B magnesium alloy via stationary shoulder friction stir processing. *J. Mater. Res. Technol.* **2022**, *17*, 3150–3156. [CrossRef]
27. Liu, C.Q.; Chen, X.H.; Zhang, W.; Zhang, Y.S.; Pan, F.S. Microstructure, creep behavior and corrosion resistance in the ultrafine-grained surface layer of Mg-6Zn-0.2Y-0.4Ce-0.5Zr alloy processed by surfacing friction treatment. *Mater. Sci. Eng. A* **2020**, *776*, 138995. [CrossRef]
28. Xie, J.; Zhang, J.; Zhang, Z.; Qiu, X.; Zhang, H.; Zhang, H.; Jiao, X.; Wu, X.; Wu, R. Corrosion behavior and mechanism of Mg-Er-Zn-Zr alloys in different states. *J. Mater. Res. Technol.* **2020**, *19*, 30–45. [CrossRef]
29. Ralston, K.D.; Fabijanic, D.; Birbilis, N. Effect of grain size on corrosion of high purity aluminium. *Electrochim. Acta* **2011**, *56*, 1729–1736. [CrossRef]
30. Liu, C.; Wang, Q.; Han, B.; Luan, J.H.; Kai, J.J.; Liu, C.T.; Wu, G.; Lu, J. Second phase effect on corrosion of nanostructured Mg-Zn-Ca dual-phase metallic glasses. *J. Magnes. Alloys* **2021**, *9*, 1546–1555. [CrossRef]
31. Baek, S.M.; Kang, J.S.; Kim, J.C.; Kim, B.; Shin, H.J.; Park, S.S. Improved corrosion resistance of Mg-8Sn-1Zn-1Al alloy subjected to low-temperature indirect extrusion. *Corros. Sci.* **2018**, *141*, 203–210. [CrossRef]
32. Yu, Z.; Ju, D.Y.; Zhao, H.Y. Effect of stress corrosion cracking at various strain rates on the electrochemical corrosion behavior of Mg-Zn-In-Sn alloy. *J. Environ. Sci.* **2013**, *25*, S50–S53. [CrossRef] [PubMed]
33. Jia, Z.; Yu, Y.Z.; Yu, B.; Fu, L.; Hu, W.Y.; Shao, Y.C. Effect of Ca and Zr Additions on Microstructure and Mechanical Properties of As-Extruded Mg-3Sn Alloy. *Materials* **2022**, *15*, 6343. [CrossRef] [PubMed]
34. Jia, Z.; Yu, B.; Fu, L. Effect of Zn and Cu Addition on Mechanical Properties of As-Extruded Mg-3Sn-1Ca Alloy. *Materials* **2022**, *15*, 4438. [CrossRef]
35. Argade, G.R.; Panigrahi, S.K.; Mishra, R.S. Effects of grain size on the corrosion resistance of wrought magnesium alloys containing neodymium. *Corros. Sci.* **2012**, *58*, 145–151. [CrossRef]
36. Gong, C.W.; Yan, X.; He, X.Z.; Su, Q.; Liu, B.S.; Chen, F.H.; Fang, D.Q. Influence of homogenization treatment on corrosion behavior and discharge performance of the Mg-2Zn-1Ca anodes for primary Mg-air batteries. *Mater. Chem. Phys.* **2022**, *280*, 125802. [CrossRef]
37. Wang, Y.J.; Zhang, Y.; Jiang, H.T. Effect of grain size uniformity and crystallographic orientation on the corrosion behavior of Mg-2Zn-1Al bar. *Mater. Charact.* **2021**, *179*, 111374. [CrossRef]
38. Fang, H.J.; Liu, H.; Yan, Y.; Luo, X.; Xu, X.C.; Chu, X.; Lu, Y.J.; Yu, K.; Wang, D.G. Evolution of texture, microstructure, tensile strength and corrosion properties of annealed Al-Mg-Sc-Zr alloys. *Mater. Sci. Eng. A* **2021**, *804*, 140682. [CrossRef]
39. Gerashi, E.; Alizadeh, R.; Langdon, T.G. Effect of crystallographic texture and twinning on the corrosion behavior of Mg alloys: A review. *J. Magnes. Alloys* **2022**, *10*, 313–325. [CrossRef]
40. Duley, P.; Bairagi, D.; Bairi, L.R.; Bandyopadhyay, T.K.; Mandal, S. Effect of microstructural evolution and texture change on the in-vitro bio-corrosion behaviour of hard-plate hot forged Mg-4Zn-0.5Ca-0.16Mn (wt%) alloy. *Corros. Sci.* **2021**, *192*, 109860. [CrossRef]
41. Pu, Z.; Song, G.L.; Yang, S.; Outeiro, J.C.; Dillon, O.W.; Puleo, D.A.; Jawahir, I.S. Grain refined and basal textured surface produced by burnishing for improved corrosion performance of AZ31B Mg alloy. *Corros. Sci.* **2012**, *57*, 192–201. [CrossRef]
42. Liu, M.; Qiu, D.; Zhao, M.C.; Song, G.; Atrens, A. The effect of crystallographic orientation on the active corrosion of pure magnesium. *Scr. Mater.* **2008**, *58*, 421–424. [CrossRef]
43. Song, G.L.; Mishra, R.; Xu, Z.Q. Crystallographic orientation and electrochemical activity of AZ31 Mg alloy. *Electrochem. Commun.* **2010**, *12*, 1009–1012. [CrossRef]
44. Liu, L.; Dong, S.; Wang, F.H.; Chen, X.B.; Dong, J. Fabrication of uniform and anti-corrosion layered double hydroxides film on Mg-Gd-Y-Zn-Zr alloy through solution pH tailoring. *Electrochim. Acta* **2022**, *411*, 140057. [CrossRef]
45. Huang, H.; Li, D.H.; Hou, F.; Du, H.Y.; Wei, H.; Liu, X.D.; Wang, Q.; Wei, Y.H. Advanced protective layer design on the surface of Mg-based metal and application in batteries: Challenges and progress. *J. Power Sources* **2022**, *542*, 231755. [CrossRef]

46. Sha, J.C.; Qiao, M.L.; Bao, J.X.; Liu, H.L.; Yin, S.Q.; Liu, W.H.; Zhao, Z.; Zhao, Z.L.; Cui, J.Z.; Zhang, Z.Q. Improving the electrochemical behaviors and discharge performance of as-rolled Mg-4Li alloys through multicomponent alloying. *J. Alloys Compd.* **2022**, *895*, 162536. [CrossRef]
47. Hanson, K.; Sankar, K.M.; Weck, P.F.; Startt, J.K.; Dingreville, R.; Deo, C.S.; Sugar, J.D.; Singh, P.M. Effect of excess Mg to control corrosion in molten $MgCl_2$ and KCl eutectic salt mixture. *Corros. Sci.* **2022**, *194*, 109914. [CrossRef]
48. Wang, C.M.; Zeng, L.M.; Ding, W.C.; Liang, T.X. Effects of minor RE (Y, La) on microstructure and corrosion behavior of TX31 alloys. *J. Mater. Res. Technol.* **2021**, *14*, 69–80. [CrossRef]
49. Bahmani, A.; Arthanari, S.; Shin, K.S. Corrosion behavior of Mg–Mn–Ca alloy: Influences of Al, Sn and Zn. *J. Magnes. Alloys* **2019**, *7*, 38–46. [CrossRef]
50. Wang, C.M.; Zeng, L.M.; Zhang, W.L.; Tang, F.Q.; Ding, W.C.; Xiao, S.F.; Liang, T.X. Enhanced mechanical properties and corrosion resistance of rolled Mg-1.5Sn-0.5Ca alloy by Ce microalloying. *Mater. Charact.* **2021**, *179*, 111325. [CrossRef]
51. Wang, X.J.; Chen, Z.N.; Guo, E.Y.; Liu, X.Q.; Kang, H.J.; Wang, T.M. The role of Ga in the microstructure, corrosion behavior and mechanical properties of as-extruded Mg–5Sn–xGa alloys. *J. Alloys Compd.* **2021**, *863*, 158762. [CrossRef]

Disclaimer/Publisher's Note: The statements, opinions and data contained in all publications are solely those of the individual author(s) and contributor(s) and not of MDPI and/or the editor(s). MDPI and/or the editor(s) disclaim responsibility for any injury to people or property resulting from any ideas, methods, instructions or products referred to in the content.